Infrared luminosity functions of AKARI Sloan Digital Sky galaxies

Mon. Not. R. Astron. Soc. **000**, 000–000 (0000) Printed 18 February 2011 (MN LATEX style file v2.2)

Infrared Luminosity Functions of AKARI-SDSS Galaxies

Tomotsugu Goto[1,2], ⋆ Stephane Arnouts[3], Matthew Malkan[4], Toshinobu Takagi[5], Hanae Inami[6], Chris Pearson[7], Takehiko Wada[5], Hideo Matsuhara[5], Chisato Yamauchi[5], Tsutomu T. Takeuchi[10,11], Takao Nakagawa[5], Shinki Oyabu[11], Daisuke Ishihara[11], David B. Sanders[1], Emeric Le Floc'h[12], Hyung Mok Lee[13], Woong-Seob Jeong[14], Stephen Serjeant[15], and Chris Sedgwick[15]

[1]*Institute for Astronomy, University of Hawaii, 2680 Woodlawn Drive, Honolulu, HI, 96822, USA*
[2]*Subaru Telescope 650 North A'ohoku Place Hilo, HI 96720, USA*
[3]*Canada France Hawaii Telescope, 65-1238 Mamalahoa Hwy, Kamuela, Hawaii 96743 USA*
[4]*Department of Physics and Astronomy, UCLA, Los Angeles, CA, 90095-1547, USA*
[5]*Institute of Space and Astronautical Science, Japan Aerospace Exploration Agency, Sagamihara, Kanagawa 252-5210*
[6]*Spitzer Science Center, California Institute of Technology, Pasadena, CA 91125, USA*
[7] *RAL Space, Rutherford Appleton Laboratory, Chilton, Didcot, Oxfordshire OX11 0QX, UK*
[8] *Institute for Space Imaging Science, University of Lethbridge,Lethbridge, Alberta T1K 3M4, Canada*
[9] *Astrophysics Group, Department of Physics, The Open University, Milton Keynes, MK7 6AA, UK*
[10]*Institute for Advanced Research, Nagoya University, Furo-cho, Chikusa-ku, Nagoya 464-8601*
[11]*Division of Particle and Astrophysical Science, Nagoya University, Furo-cho, Chikusa-ku, Nagoya 464-8602, Japan*
[12]*CEA-Saclay, Service d'Astrophysique, France*
[13]*Department of Physics & Astronomy, FPRD, Seoul National University, Shillim-Dong, Kwanak-Gu, Seoul 151-742, Korea*
[14]*Korea Astronomy and Space Science Institute 61-1, Hwaam-dong, Yuseong-gu, Daejeon, Republic of Korea 305-348*
[15]*Astrophysics Group, Department of Physics, The Open University, Milton Keynes, MK7 6AA, UK*

18 February 2011

ABSTRACT

By cross-correlating AKARI all sky survey in 6 infrared (IR) bands (9, 18, 65, 90, 140, and 160μm) with the SDSS galaxies, we identified 2357 infrared galaxies with a spectroscopic redshift. This is not just one of the largest samples of local IR galaxies, but AKARI provides crucial FIR bands in accurately measuring galaxy SED across the peak of the dust emission at $> 100\mu m$. By fitting modern IR SED models to the AKARI photometry, we measured the total infrared luminosity (L_{IR}) of individual galaxies.

Using this L_{IR}, we constructed the luminosity functions of infrared galaxies at a median redshift of z=0.031. The LF agrees well with that at z=0.0082 (the RBGS), showing smooth and continuous evolution toward higher redshift LFs measured in the AKARI NEP deep field. By integrating the IR LF weighted by L_{IR}, we measured the local cosmic IR luminosity density of Ω_{IR}= $(3.8^{+5.8}_{-1.2}) \times 10^8$ $L_\odot$Mpc^{-3}.

We separate galaxies into AGN (active galactic nuclei), star-forming, and composite by using the $[NII]/H\alpha$ vs $[OIII]/H\beta$ line ratios. The fraction of AGN shows a continuous increase with increasing L_{IR} from 25% to 90% at 9< $logL_{IR}$ <12.5. The SFR$_{H\alpha}$ and $L_{[OIII]}$ show good correlations with L_{IR} for SFG (star-forming galaxies) and AGN, respectively. The self-absorption corrected Hα/Hβ ratio shows a weak increase with L_{IR} with a substantial scatter. When we separate IR LFs into contributions from AGN and star-forming galaxies (SFG), the AGN contribution becomes dominant at $L_{IR} > 10^{11}L_\odot$, coinciding the break of the both SFG and AGN IR LFs. At $L_{IR} \leqslant 10^{11}L_\odot$, SFG dominates IR LFs. Only 1.1$\pm$0.1% of Ω_{IR} is produced by LIRG ($L_{IR} > 10^{11}L_\odot$), and only 0.03$\pm$0.01% is by ULIRG ($L_{IR} > 10^{12}L_\odot$) in the local Universe. Compared with high redshift results from the AKARI NEP deep survey, we observed a strong evolution of Ω_{IR}^{SFG} $\propto$(1+z)$^{4.1\pm0.4}$ and Ω_{IR}^{AGN} $\propto$(1+z)$^{4.1\pm0.5}$. Our results show all of our measured quantities (IR LFs, L^*, Ω_{IR}^{AGN}, Ω_{IR}^{SFG}) show smooth and steady increase from lower redshift (the RBGS) to higher redshift (the AKARI NEP deep survey).

Key words: galaxies: evolution, galaxies:interactions, galaxies:starburst, galaxies:peculiar, galaxies:formation

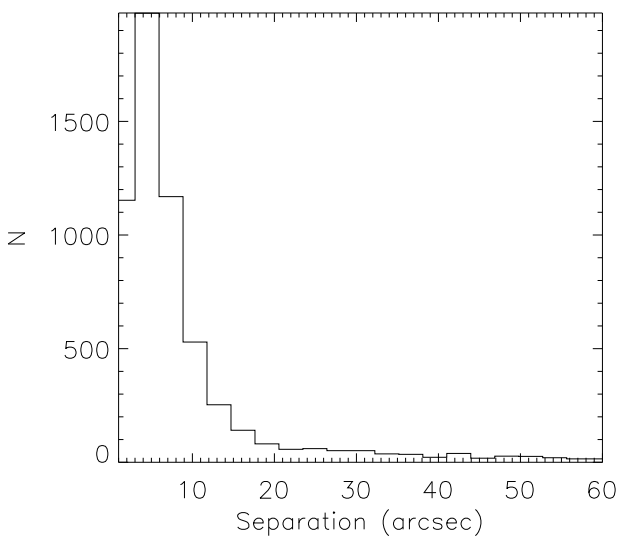

Figure 1. Angular separation between the AKARI FIS and SDSS positions. We use galaxies matched within 20 arcsec for LFs.

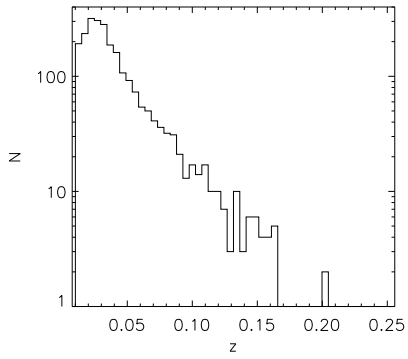

Figure 2. Redshift distribution of the AKARI-SDSS galaxies.

1 INTRODUCTION

To understand the cosmic history of star formation and AGN (active galactic nuclei), it is vital to understand infrared (IR) emission; the more intense star formation, the more deeply it is embedded in the dust, hence, such star formation is not visible in UV but in the infrared. Similarly, AGN evolutionary scenarios predict that AGN are heavily obscured at their youngest, compton-thick stage (Treister, Urry, & Virani 2009). The Spitzer and AKARI satellites revealed a great deal of infrared emission in the high-redshift Universe, showing strong evolution in the infrared luminosity density (Le Floc'h et al. 2005; Pérez-González et al. 2005; Babbedge et al. 2006; Caputi et al. 2007; Magnelli et al. 2009; Gruppioni et al. 2010; Rodighiero et al. 2010). For example, at z=1, Goto et al. (2010a) estimated 90% of star formation activity is hidden by dust.

However, to investigate evolution of IR LF, these high-redshift studies need a good comparison sample at z=0. Even today, the often used is the IRAS LFs (Rush, Malkan and Spinoglio 1993; Sanders et al. 2003; Goto et al. 2010c) from 1980s, with only several hundred galaxies. In addition, for more than 25 years, bolometric infrared luminosities ($L_{IR,8-1000\mu m}$) of local galaxies have been estimated using equation in Pérault (1987), which is a simple polynomial, obtained assuming a simple blackbody and dust emissivity. Furthermore, the reddest filter of IRAS is $100\mu m$, which does not span the peak of the dust emission for most galaxies, leaving a great deal of uncertainty. A number of studies found cold dust that cannot be detected with the IRAS. For example, Dunne & Eales (2001) detected such cold dust with $T \sim$ 20K using Scuba 450,850 μm flux. Symeonidis et al. (2009) detected cold galaxies with SED peaks at longer wavelengths using Spitzer/MIPS. These results cast further doubt on L_{IR} estimated using only $< 100\mu$m photometry. More precise estimate of local L_{IR} and thus the local IR luminosity function (LF) have been long awaited, to be better compared with high redshift work and to understand where the end-point of the cosmic IR density evolution is.

AKARI, the Japanese infrared satellite (Murakami et al. 2007), provides the first chance to rectify the situation since IRAS; AKARI performed an all-sky survey in two mid-infrared bands (centered on 9 and 18 μm) and in four far-infrared bands (65,90, 140, and 160μm). Its 140 and 160μm sensitivities are especially important to cover across the peak of the dust emission, allowing us to accurately measure the Rayleigh-Jeans tail of the IR emission.

Using deeper data and modern models, in this work, we aim to measure local L_{IR}, and thereby the IR LF. By matching the AKARI IR sources with the SDSS galaxies, our sample contains $\sim$2357 IR galaxies. Compared to the previous work (Sanders et al. 2003; Goto et al. 2010c), the sample is several times larger, allowing us to accurately measure IR LF of the local Universe. The optical spectra of the SDSS also allows us to separate IR emission from AGN and star-forming galaxies. This work provides us an important local benchmark to base our evolution studies at high redshift both by the current AKARI, Spitzer, and Herschel satellites, and by next-generation IR satellites such as WISE, JWST, and SPICA. Following Sanders et al. (2003), we adopt a cosmology with $(h, \Omega_m, \Omega_\Lambda) = (0.75, 0.3, 0.7)$.

2 DATA AND ANALYSIS

2.1 AKARI-SDSS sample

AKARI (Murakami et al. 2007) performed an all-sky survey in two mid-infrared bands (centered on 9 and 18 μm) and in four far-infrared bands (65,90,140, and 160μm). In this work, we use the version 1 of the AKARI/IRC point source catalog and the AKARI/FIS bright source catalog, which is selected in 90μm. The 5 σ sensitivities in the AKARI IR filters ($S9W, L18W, N60, WS, WL$ and $N160$) are 0.05, 0.09, 2.4, 0.55, 1.4, and 6.3 Jy (Ishihara et al. 2010; Yamamura et al. 2009). In addition to the much improved sensitivity and spatial resolution over its precursor (the IRAS all-sky survey), the presence of 140 and 160μm bands is crucial to measure the peak of the dust emission in the FIR wavelength, and thus the L_{IR} of galaxies.

To measure L_{IR}, we need spectroscopic redshift of individual galaxies. We have cross-correlated the AKARI FIS bright source catalog with the SDSS DR7 galaxy catalog (Abazajian et al. 2009), which is the largerst redshift survey in the local Universe to date.

We used a matching radius of 20 arcsec, as shown in Fig.1. This radius is determined based mainly on the positional accuracy of the AKARI FIR sources since for the SDSS, positional accuracy is less than 0.1" to the survey limit ($r \sim$22 Pier et al. 2003). AKARI's PSF size in the 90μm filter is 39$\pm$1". The astrometric

accuracy of the AKARI FIS bright source catalog is 3.8" in cross-scan direction and 4.8" in in-scan direction (Yamamura et al. 2009). The 20" radius also accounts for the physiscal shift that could be present between the peaks of the FIR and the optical emission. At the median redshift of z=0.031, 20" corresponds to 12 kpc. The source density of the SDSS main spectroscopic galaxies is 92 deg^{-2} (Strauss et al. 2002). Therefore, within the 20" around each AKARI sources, 0.009 of background galaxies are expected to be present, i.e., less than 1% of our sources are expected to be a chance coincidence, which should not affect our estimate of the LFs. See (Sutherland & Saunders 1992) for a maximum likelihood approach to this.

We do not use galaxies at $z < 0.01$ since (i) at such a low velocity, uncertainty from peculiar velocity is too large to estimate distance from spectroscopic redshift, and (ii) the AKARI's photometry of largely extended objects is not finalized yet. We also remove galaxies at $z \geqslant 0.3$ to avoid too much evolutionary effect within the redshift range. We also use SDSS galaxies with extinction corrected $r_{petro} \leqslant 17.7$, where the SDSS main galaxy spectroscopic target selection can be considered complete. To obtain reliable LFs, we only use AKARI sources with $S_{90\mu m} > 0.7Jy$, where completeness is greater than 80%. Among these, 99% of sources have high quality flag of `fqual=3` in $90\mu m$. 67% of AKARI sources with $S_{90\mu m} > 0.7Jy$ in the area covered by the SDSS had an optical counterpart. The rest of the sources are either stars or galaxies fainter than $r_{petro} = 17.7$, which are property accounted for the LF computation in Section 3.1.

Previous sample of local IR LFs was based on IRAS $S_{60\mu m}$ flux, and thus, it has been a concern that colder galaxies, whose FIR emission peak at larger wavelengths, might have been missed in the sample. Our sample is selected using $S_{90\mu m}$ flux, and thus, more robust to such a selection bias.

We found cross-matches of 2357 galaxies, with which we will measure IR LFs. Among these, 97, 98, and 87% of sources have measured flux in 65, 140 and 160μm. For these source the AKARI IRC catalog is also cross-matched. Only 0.8% of FIS-SDSS sources do not have an IRC counterpart within 20 arcsec. Fig.2 shows a redshift distribution of the sample. The number of galaxies used are similar to the IRAS based work by Goto (2005), despite the twice increase in the optical (SDSS) sample. This is due to more stringent cross-matching criterion we used. AKARI's improved astrometry allowed us to remove ambiguous cross-ids. Nevertheless, thanks to the large sky coverage of the SDSS and AKARI surveys, this is one of the largest number of galaxies used to construct IR LFs. For example, previous local IR LFs are based on $\sim$600 galaxies (Sanders et al. 2003; Goto et al. 2010c) .

2.2 Estimating total IR luminosity

For these galaxies, we estimated total IR luminosities (L_{IR}) by fitting the AKARI photometry with SED templates. We used the `LePhare` code[1] to fit the infrared part ($>7\mu$m) of the SED. We fit our AKARI FIR photometry with the SED templates from Chary & Elbaz (CHEL hereafter 2001), which showed most promising results among SED models tested by Goto et al. (2010c). It is a concern that the CHEL models do not include SEDs for AGN. However, we show later in Section 2.3 that this is not a major problem using observed data. We did not include IRAS photometry in the SED fit partly because the better spatial resolution of AKARI often resolves background cirrus and nearby companion better (Jeong et al. 2007), and partly because not all of the AKARI sources are detected with the IRAS due to the difference in flux limits. Although the shape of these SEDs are luminosity-dependent, the large baseline from AKARI observations ($S9W, L18W, N60, WS, WL$ and $N160$) allows us to adopt a free scaling to obtain the best SED fit, which is then rescaled to derive L_{IR}. To be precise, we only used $\geqslant 65\mu$m flux to free scale the SEDs since mid-IR bands can sometimes be affected by the stellar emission. For those sources with low quality flag (`fqual=1`), we adopted a minimum error of 25%. In this work, L_{IR} is measured in the wavelength range of 8-1000μm. Fig. 3 shows L_{IR} as a function of spectroscopic redshift.

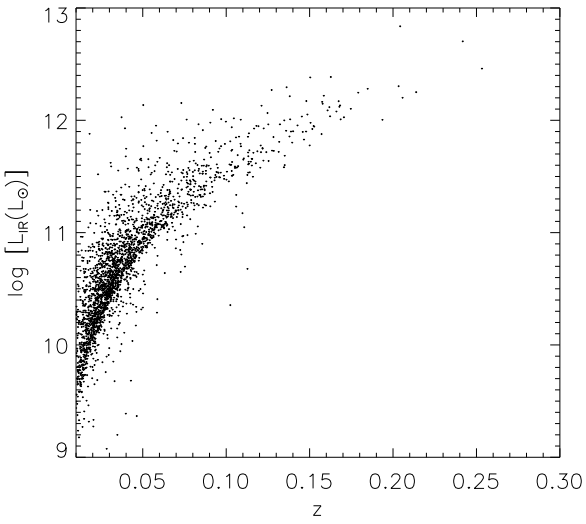

Figure 3. L_{IR} measured by the AKARI as a function of spectroscopic redshift.

2.3 AGN/SFG separation

One has to be careful that two different physical mechanisms contribute to total infrared emission of galaxies: one by star-formation and the other by AGN. It is therefore fundamental to separate IR contribution from these two different physics, to understand the evolution of the star-formation and AGN activity. However, this has been notoriously difficult and has been a subject of active debate over the last decades. Many AGN/SF separation methods have been proposed such as X-ray, radio luminosity, optical line ratios, PAH strengths, submm properties and so on (Zhu et al. 2008; Sajina et al. 2008; LaMassa et al. 2010). Often, not all of the indicators do not agree one another, partly due to complicated nature of IR sources (multiple core, composite ...etc).

In this work, since we have optical spectra of individual galaxies, we use $[NII]/H\alpha$ vs $[OIII]/H\beta$ line ratios to classify galaxies into AGN or SFG (star-forming galaxies). In Fig.4, we plot $[NII]/H\alpha$ against $[OIII]/H\beta$ line ratios. The black contours show the distribution of all emission line galaxies in the SDSS, regardless of the AKARI detection. The dotted and dashed lines are the AGN/SFG separation criteria presented by Kewley et al. (2001) and Kauffmann et al. (2003), respectively. We regard galax-

[1] http://www.cfht.hawaii.edu/~ arnouts/lephare.html

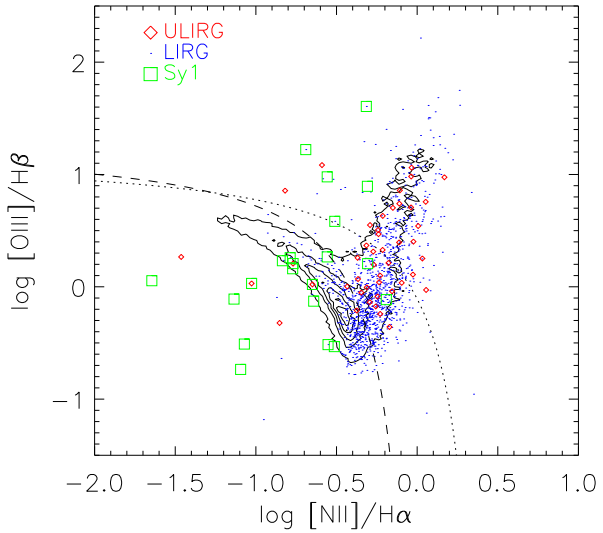

Figure 4. Emission line ratios used to select AGNs from our sample. The contour shows distribution of all galaxies in the SDSS with $r < 17.77$ (regardless of IR detection). The dotted line is the criterion between starbursts and AGNs described in Kewley et al. (2001). The dashed line is the criterion by Kauffmann et al. (2003). Galaxies with line ratios higher than the dotted line are regarded as AGNs. Galaxies below the dashed line are regarded as star-forming. Galaxies between the dashed and dotted lines are regarded as composites. The blue and red dots are for ULIRGs, LIRGs, respectively. The green squares are Seyfert 1 galaxies identified by eye-balling optical spectra.

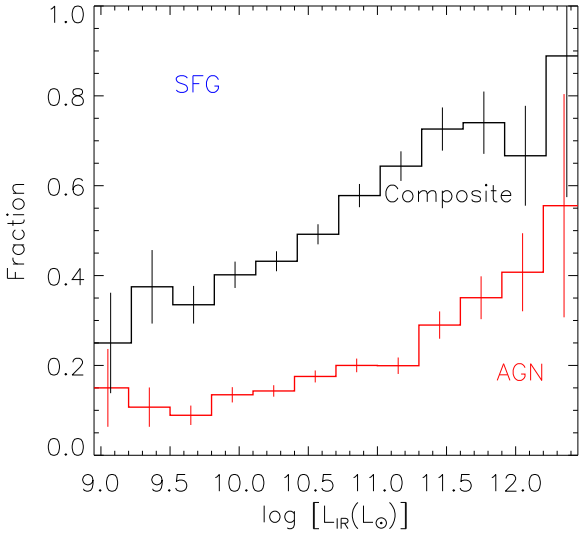

Figure 5. Fractions of AGN and composite galaxies as a function of L_{IR}. AGN are classified using Kewley et al. (2001) among galaxies with all 4 lines measured. Composite galaxies include those classified as AGN using Kauffmann et al. (2003).

ies above the dotted line as AGN, below the dashed line as SFG, and those in between as composite galaxies.

Although these line diagnosis criteria work well for narrow-line AGN, they could be problematic for broad-line AGN. Although, in principle, one could separate narrow line components from broad-line by multiple-line fitting, it is often difficult with weak lines on noisy spectra. To see how well broad line AGN are classified in Fig.4, one of us (M.M.) has eyeballed all emission line IR galaxies with FWHM(Hα) greater than FWHM([OIII]) by more than 150 km/s. We identified 22 broad-line AGN, which are shown in green squares in Fig.4. As expected, the broad-line AGN are scattered everywhere in the Figure and escapes from the above criteria. Therefore, we manually overruled the classification of these broad-line AGN, and treated them as AGN in the rest of the paper, regardless of the line ratios in Fig.4. In this process, we also came across 20 narrow line AGN (although these are not a complete sample). They were successfully classified as AGN in Fig.4.

In Fig.4, ULIRGs and LIRGs are marked with red diamonds and blue dots, respectively. It is interesting that majority of (U)LIRGs are aligned along the AGN branch of the diagram, implying the AGN fraction is high among (U)LIRGs. This is more clearly seen in Fig.5, where we plot fractions of AGN as a function of L_{IR}. The red solid line shows fractions of AGN only, and the black dotted line includes composite galaxies. Note that the fractions do not include completely obscured sources in optical for both SFG and AGN. The fractions of AGN (including composites) increase from 15% (25%) at logL_{IR}=9.0 to 55% (90%) at logL_{IR}=12.3. This results agree with previous AGN fraction estimates (Goto 2005; Yuan, Kewley, & Sanders 2010; Kartaltepe et al. 2010). Improvement in this work is that due to much larger statistics, we were able to show fractions of AGN in much finer luminosity bins, more accurately quantifying the increase. Especially, a sudden increase of f_{AGN} at logL_{IR} >11.3 is notable due to the increased statistics in this work.

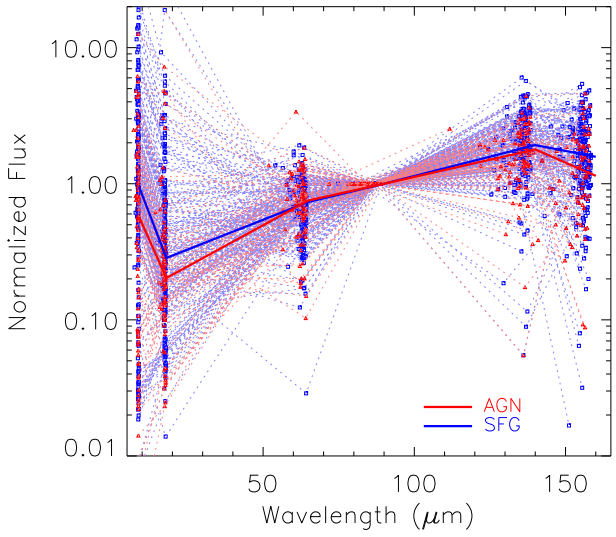

Figure 6. SEDs of AGN (red triangles) and SFG (blue squares). The red and blue solid lines connect median values for AGN and SFG, respectively. Note that only galaxies detected in all the 6 AKARI bands are shown here. The flux are normalized at 90μm.

Having AGN/SFG classified, in Fig.6, we show restframe SEDs of AGN (red triangles) and SFG (blue squares), separately. Note that only galaxies detected in all the 6 AKARI bands are shown here. The flux are normalized at 90μm. The solid lines connect median points for each sample. In Fig.6, there is no significant

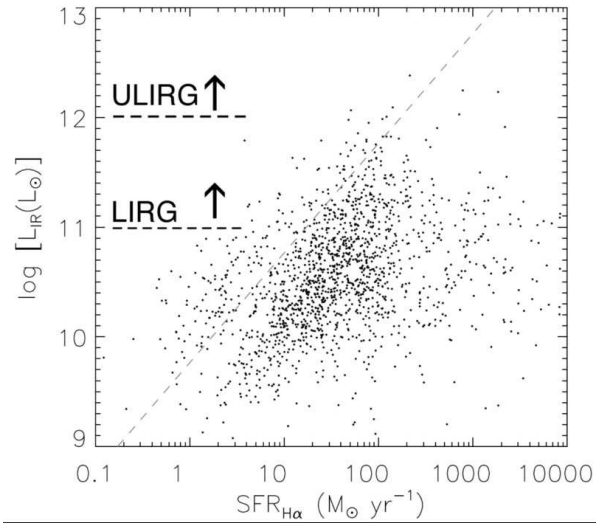

Figure 7. The SFR computed from the Hα emission line is plotted against the total infrared luminosity (L_{IR}). The Hα lines are corrected for stellar absorption and extinction using the Balmer decrement. AGNs are excluded from this figure using Fig.4.

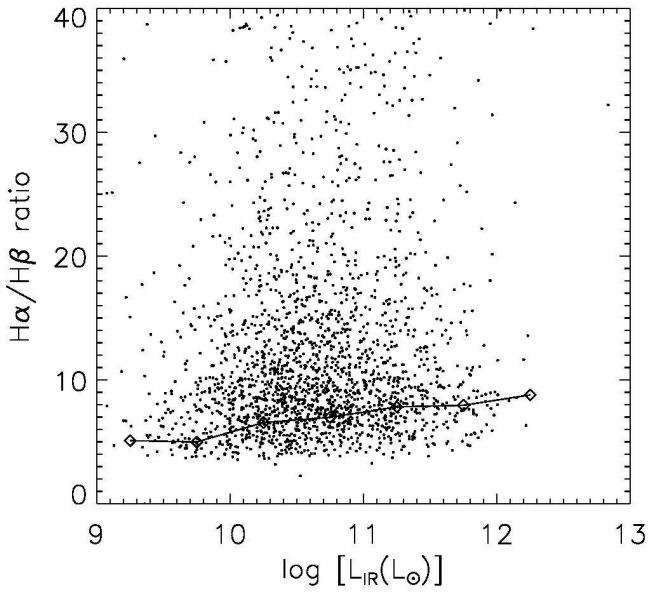

Figure 8. The self-absorption corrected Hα/Hβ ratios are shown against L_{IR} for SFG. The solid line connects median values.

difference between AGN and SFG SEDs. This has two implications: although the CHEL SED models do not include SEDs for AGNs, the SED fit can be performed using the galaxy SED models. At the same time, we need to be careful that although we selected AGN based on the optical line ratios, infrared SEDs of these optically-selected AGN can be dominated by star-formation activity in the AGN host galaxy.

In Fig.7, we show star formation rate (SFR) computed from the self-absorption and extinction corrected $H\alpha$ flux (Goto 2005) against L_{IR} for SFGs. The SFR is also corrected for the fiber loss of the SDSS spectrograph. There is a correlation, but compared with the well-known relation by Kennicutt (1998), there is a significant offset. This might warn us a simple application of Kennicutt (1998)'s law to IR luminous galaxies. Kennicutt (1998)'s sample was dominated by more regular (less IR luminous) spiral galaxies, whose L_{IR} might stem from cool cirrus clouds warmed by older stars. This might not be the case for vigorously star-forming LIRG and ULIRGs with hot dust.

In Fig.8, we plot the self-absorption corrected $H\alpha$/ $H\beta$ ratio as a function of L_{IR} for SFG. Although the median in the solid line shows a slight increase with increasing $H\alpha$/ $H\beta$ ratio, but with a large scatter, suggesting that not only L_{IR} decides the dust extinction in galaxies.

In Fig.9 we plot L_{IR} vs $L_{[OIII]}$. Only objects classified as AGN are shown here. Both of these luminosities are considered to be good indicators of the AGN power, and there is a recognizable correlation, however, with a significant scatter. The exact reason of the scatter is unknown but possible causes include contamination from HII regions, cirrus emission, shocks, and emission from very little narrow-line region directly powered by an accreting black hole.

In Fig.10, we show restframe $u-r$ vs M_r color-magnitude diagram. We used Blanton et al. (2003, v4_1) for k-correction. The contours show the distribution of all SDSS galaxies with $r < 17.7$ regardless of IR detection. ULIRGs and LIRGs do not follow neither the red-sequence at $u-r \sim 2.6$ nor blue cloud at $u-r < 2.0$,

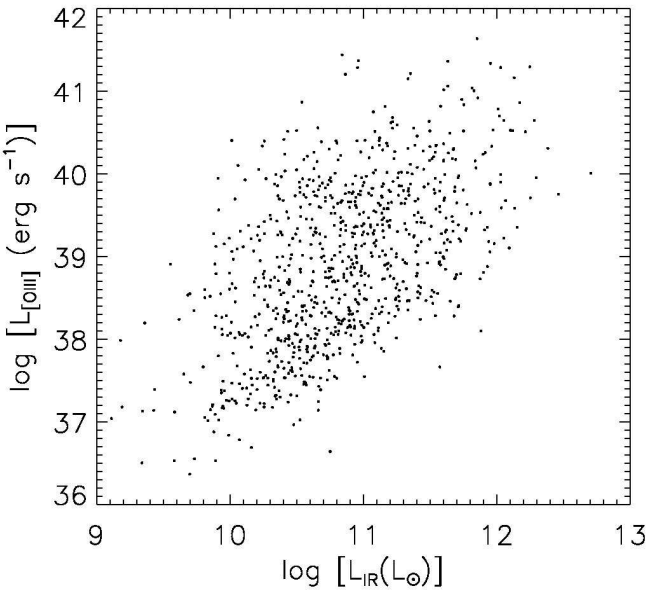

Figure 9. Luminosity of the [OIII](5008Å) emission line is plotted against total infrared luminosity for AGNs. Only objects classified as AGN are shown here.

but widely distributed in the $u-r$ color. As expected, ULIRGs are more luminous in M_r than LIRGs.

The red squares, green diamonds, and blue dots are for AGN, composite, and SF IR galaxies classified using Fig.4. These IR galaxies also show wide distribution in Fig.10, with AGN slightly brighter than the composite, reflecting the fact that the AGN fractions are higher for more luminous objects (Fig.5). The SFG are slightly more extended to bluer clouds than AGN and the compos-

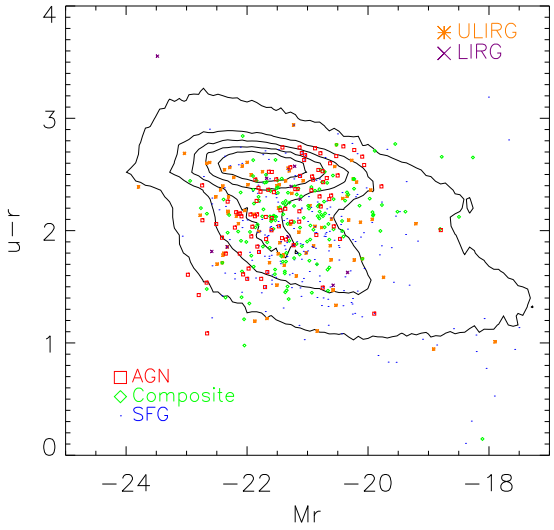

Figure 10. Restframe $u-r$ vs Mr color-magnitude diagram. The contours show the distribution of all SDSS galaxies with $r < 17.7$. The orange stars and crosses denote ULIRGs and LIRGs in our sample. The red square, green diamond, and blue dots are for AGN, Composite, and SF IR galaxies classified using Fig.4.

ite. These distributions are consistent with AGN and IR galaxies populate the so-called "green valley" between red-sequence and blue clouds (Smolčić 2009; Schawinski et al. 2010). Perhaps physical reasons deciding $u-r$ color are different for AGNs and SFG. For example, dust-reddening might play a significant role for SFG, especially infrared luminous ones. For AGN, lack of gas in red-sequence galaxies, and dominance of HII regions in blue-cloud galaxies may push AGN into the green valley.

We caution readers that our AGN/SFG classification is by no means complete, but merely one attempt. In reality most of galaxies have both AGN and star-formation, and thus contribution to L_{IR} and $L_{[OIII]}$ from both components. When one is dominant, it is difficult to assess a contribution from the other, which inevitably becomes a contamination to the former. Recently, it has been reported that to fit FIR SED of AGN dominant galaxies, one always need a starburst component, even for quasars (Shao et al. 2010; Hatziminaoglou et al. 2010; Pozzi et al. 2010). In this sense, our L_{IR} of AGN include IR emission from an AGN host galaxy. The latter might be dominant in FIR wavelength. Those galaxies with line ratios consistent to be LINERs are treated as AGN in this paper, but their emission may have nothing to do with an accreting black hole, instead may be from shocks or something else. Therefore, it is possible that these classified as AGN in this paper still have significant infrared emission from host galaxies, instead of central black holes. To make the matter worse, it is additional unknown how many completely obscured galaxies we miss in our optical classification for both AGN and SFG. While this work had only optical line ratios for classification, the final conclusion must be based on multi-wavelength data.

3 INFRARED LUMINOSITY FUNCTIONS

3.1 The 1/$V_{\rm max}$ method

With accurately measured L_{IR}, we are ready to construct IR LFs. Since our sample is flux-limited at $r = 17.7$ and $S_{90\mu m} = 0.7Jy$, we need to correct for a volume effect to compute LFs. We used the $1/V_{\rm max}$ method (Schmidt 1968). An advantage of the $1/V_{\rm max}$ method is that it allows us to compute a LF directly from data, with no parameter dependence or a model assumption. A drawback is that it assumes a homogeneous galaxy distribution and thus is vulnerable to local over-/under-densities (Takeuchi, Yoshikawa, & Ishii 2000).

A comoving volume associated to any source of a given luminosity is defined as $V_{\rm max} = V_{z_{\rm max}} - V_{z_{\rm min}}$, where $z_{\rm min}$ is the lower limit of the redshift and $z_{\rm max}$ is the maximum redshift at which the object could be seen given the flux limit of the survey. In this work, we set $z_{\rm min}$=0.01 since at a very small redshift, an error in redshift measurement is dominated by a peculiar motion, and thus, L_{IR} also has a large error.

For the infrared detection limit, we used the same SED templates (Chary & Elbaz 2001) as we used to compute L_{IR} for k-correction to obtain the maximum observable redshift from the $S_{90\mu m}$ flux limit. For optical detection limit, we used Blanton et al. (2003, v4_1) for k-correction. We adoped a redshift where galaxies become fainter than eithter r- of $S_{90\mu m}$-flux limit as $z_{\rm max}$.

For each luminosity bin then, the LF is derived as

$$\phi = \frac{1}{\Delta L}\sum_i \frac{1}{V_{{\rm max},i}} w_i, \quad (1)$$

,where $V_{\rm max}$ is a comoving volume over which the ith galaxy could be observed, and ΔL is the size of the luminosity bin, and w_i the completeness correction factor of the ith galaxy. Note that the $V_{\rm max}$ method considers both the optical and IR flux limits. Therefore, even an IR source with $r > 17.7$, a detectable volume of such sources is properly considered by the $V_{\rm max}$ method as long as IR sources with the same optical-to-IR ratio can be detected at a lower redshift. See Appendix of Serjeant et al. (2001) and Avni & Bahcall (1980) for more details of a multivariate $V_{\rm max}$ method. A very obscured IR galaxy (with $r > 17.7$ even at the lowest redshift of z=0.01), however, would have a detectable volume of zero, and thus, would not be included in the LF computation. The number density of such obscured IR galaxies is a matter of interest itself, but requires deeper optical data. Although we cannot test deeper r-band criterion since the SDSS spectroscopic survey stops the current limit, we can test a brighter r-band criterion. We computed the LF using a brighter r-band criterion by one magnitude, at $r < 16.7$. The resulting LF was noisier due to the reduced number of galaxies used, but essentially the same as the LF presented in the following sections. The test suggests that the $V_{\rm max}$ method works well. We used completeness correction measured in the FIS bright source catalog release note for $S_{90\mu m}$ flux. This correction is 25% at maximum, since we only use the sample where the completeness is greater than 80%. Completeness correction in terms of sky coverage of both surveys is taken into account.

3.2 Monte Carlo simulation

Uncertainties in the LF values stem from various factors such as the finite numbers of sources in each luminosity bin, the k-correction uncertainties, and the flux errors. To compute these errors we performed Monte Carlo simulations by creating 150 simulated cata-

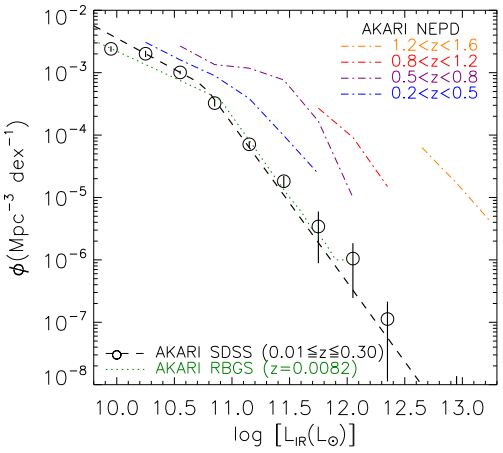

Figure 11. Infrared luminosity function of AKARI-SDSS galaxies. The L_{IR} is measured using the AKARI 9,18,65,90,140 and 160μm fluxes through an SED fit. Errors are computed using 150 Monte Carlo simulations, added by Poisson error. The dotted lines show the best-fit double-power law. The green dotted lines show IR LF at z=0.0082 by Goto et al. (2010c). The dashed-dotted lines are higher redshift results from the AKARI NEP deep field (Goto et al. 2010a).

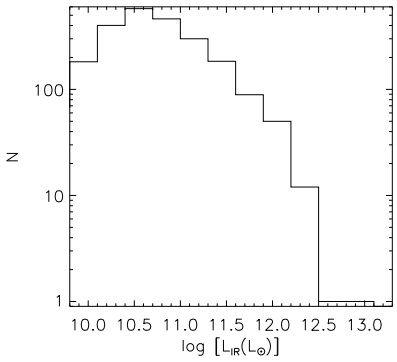

Figure 12. An infrared luminosity histogram of galaxies used to compute Fig.11.

logs, where each catalog contains the same number of sources, but we assign each source new fluxes following a Gaussian distribution centered at fluxes with a width of a measured error. Then we measured errors of each bin of the LF based from the variation in the 150 simulations. These estimated errors are added in quadrature to the Poisson errors in each LF bin.

3.3 IR luminosity function

In Fig.11, we show infrared LF of the AKARI-SDSS galaxies, followed by Fig.12, which shows number of galaxies used to compute the LF. The median redshift of our sample galaxies is z=0.031. Overplotted in green dotted lines is IR LF of RBGS at z=0.0082 but with re-measured L_{IR} based on the AKARI 6-band photometry (Goto et al. 2010c). Our LF agrees very well with that from the RBGS (Sanders et al. 2003; Goto et al. 2010c). Although it was a concern that the RBGS was $S_{60\mu m}$ selected, the agreement suggests the selection does not affect the total IR LF, perhaps because

Table 1. Best double power-law fit parameters for the AKARI LFs.

Sample	L^*_{IR} ($L_\odot$)	ϕ^*(Mpc^{-3}dex^{-1})	α (faint-end)	β (bright-end)
Total	$5.7\pm0.2\times10^{10}$	0.00062±0.00002	1.99±0.09	3.54±0.09
SFG	$5.0\pm0.2\times10^{10}$	0.00043±0.00003	1.8±0.1	3.5±0.3
AGN	$4.3\pm0.2\times10^{10}$	0.0004±0.0001	1.4±0.1	3.1±0.2

Table 2. Local IR luminosity densities by all galaxies, ULIRGs and LIRGs.

Sample	Ω^{Total}_{IR} ($L_\odot$Mpc^{-3})	$\Omega^{LIRG}_{IR}(L_\odot Mpc^{-3})$	$\Omega^{ULIRG}_{IR}(L_\odot Mpc^{-3})$
Total	$3.8^{+5.8}_{-1.2}\times10^8$	$4.2^{+0.7}_{-0.8}\times10^6$	$1.2^{+0.5}_{-0.4}\times10^5$
SFG	$5.9^{+1.4}_{-1.3}\times10^7$	$2.1^{+0.7}_{-0.8}\times10^6$	$1.4^{+0.2}_{-0.2}\times10^5$
AGN	$1.9^{+0.5}_{-0.7}\times10^7$	$1.9^{+0.5}_{-0.5}\times10^6$	$2.5^{+1.3}_{-0.9}\times10^5$

$60\mu m$ is close to the peak of the dust emission and captures most IR galaxies. Dotted lines show higher redshift results from the AKARI NEP Deep field (Goto et al. 2010a). Our results (open circles) agree with that from z=0.0082, and show smooth evolution toward higher redshift. The faint-end slope of our sample agrees well with immediately higher/lower redshift LFs.

Following Sanders et al. (2003), we fit an analytical function to the LFs. In the literature, IR LFs were fit better by a double-power law (Babbedge et al. 2006; Goto et al. 2010a,c) or a double-exponential (Pozzi et al. 2004; Takeuchi et al. 2006; Le Floc'h et al. 2005) than a Schechter function, which steeply declines at the high luminosity and underestimates the number of bright galaxies. In this work, we fit the IR LFs using a double-power law (Babbedge et al. 2006) as shown below.

$$\Phi(L)dL/L^* = \Phi^* \left(\frac{L}{L^*}\right)^{1-\alpha} dL/L^*, \quad (L < L^*) \tag{2}$$

$$\Phi(L)dL/L^* = \Phi^* \left(\frac{L}{L^*}\right)^{1-\beta} dL/L^*, \quad (L > L^*) \tag{3}$$

Free parameters are L^* (characteristic luminosity, $L_\odot$), ϕ^* (normalization, Mpc^{-3}), α, and β (faint and bright end slopes), respectively. The best-fit values are summarized in Table 1. In Fig.11, the dashed line shows the best-fit double-power law. The local LF has a break at L^*=$5.7\pm0.2\times10^{10}L_\odot$. Understanding how this break (L^*) evolves as function of cosmic time, and what causes the break is fundamental to galaxy evolution studies. This work provides an important benchmark in the local Universe.

3.4 Bolometric IR luminosity density based on the IR LF

One of the primary purposes in computing IR LFs is to estimate the IR luminosity density, which in turn is a good estimator of the dust-hidden cosmic star formation density (Kennicutt 1998), once the AGN contribution is removed. The bolometric IR luminosity of a galaxy is produced by thermal emission of its interstellar matter. In SF galaxies, the UV radiation produced by young stars heats the interstellar dust, and the reprocessed light is emitted in the IR. For this reason, in star-forming galaxies (SFG), the bolometric IR luminosity is a good estimator of the current SFR (star formation rate) of the galaxy.

Once we measured the LF, we can estimate the total infrared luminosity density by integrating the LF, weighted by the lumi-

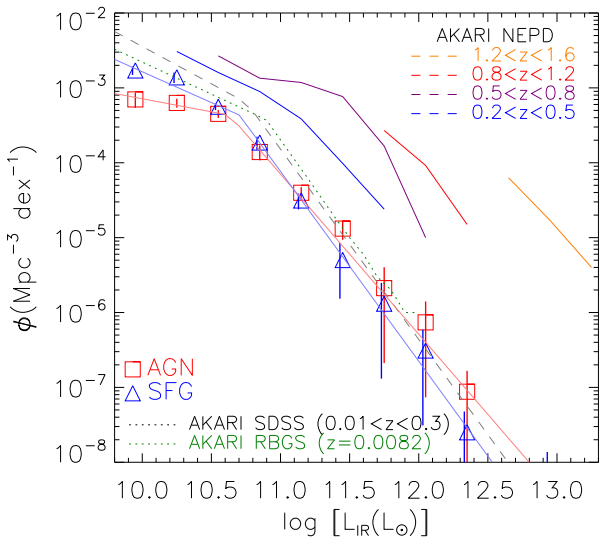

Figure 13. IR LF is separated for star-forming galaxies (blue triangles) and AGN (red squares), using classification in Fig.4. Total IR LF in Fig.11 is shown with the black dotted lines.

nosity. We used the best-fit double-power law to integrate outside the luminosity range in which we have data, to obtain estimates of the total infrared luminosity density, Ω_{IR}. Note that outside of the luminosity range we have data ($L_{IR} > 10^{12.5} L_\odot$ or $L_{IR} < 10^{9,8} L_\odot$), the LFs are merely an extrapolation and thus uncertain.

The resulting total luminosity density is Ω_{IR}= $(3.8^{+5.8}_{-1.2}) \times 10^8$ $L_\odot$Mpc^{-3}. Errors are estimated by varying the fit within 1σ of uncertainty in LFs. Out of Ω_{IR}, 1.1±0.1% is produced by LIRG ($L_{IR} > 10^{11} L_\odot$), and only 0.03±0.01% is by ULIRG ($L_{IR} > 10^{12} L_\odot$). Although these fractions are larger than z=0.0081, still a small fraction of Ω_{IR} is produced by luminous infrared galaxies at z=0.031, in contrast to high-redshift Universe. We will discuss the evolution of Ω_{IR} in Section 4.1.

3.5 AGN/SFG IR LF

Once we separated individual galaxies into AGN/SFG, we can construct LFs of each sample. However, we caution again that our L_{IR} of AGN is total infrared emission of optically-selected AGN, and thus, it includes infrared emission from AGN host galaxies. In Fig.13, we show LFs separately for AGN (red squares) and SFG (blue triangles). Composite galaxies are included in the AGN LF. The total IR LF shown in Fig.11 is also shown for comparison in the gray dashed line. It is interesting that both AGN and SFG IR LFs have a break at around log$L_{IR} \sim 11.0$. Then, the IR luminosity density of AGN exceeds that of SFG at log$L_{IR} > 11.0$, with flatter slope toward the brigher end. In contrast, the faint-end slope is steeper for SFG.

Next, we fit the double-power law (Eqs. 2 and 3) to the AGN and SF IR LFs, exactly as we did for the total IR LF in Fig.11. The best-fit parameters are summarized in Table 1. As we mentioned above, the most notable difference is at the bright- and faint-end slopes, where the AGN and SFG LFs dominate, respectively. The L^* of AGN is slightly brighter than that of SFG.

One of the pioneers in IR AGN LF is Rush, Malkan and Spinoglio (1993), who selected 893 IR galaxies (of which 118 are AGN) from IRAS 12μm to minimize wavelength-dependent selection biases towards bluer Seyfert 1 nuclei and redder embedded AGN (Spinoglio & Malkan 1989). Despite small differences such as selection, AGN classification, and L_{IR} based on the IRAS, their total IR LF of AGN in their Fig.9 is in very good agreement with ours, showing the same AGN dominance at larger L_{IR}.

What do these differences in LFs bring to the IR luminosity density, Ω_{IR}, by AGN and SFG? We estimate the total infrared luminosity density by integrating the LFs weighted by the luminosity, separately for AGN and SFG. We used the double power law outside the luminosity range in which we have data, to obtain estimates of the total infrared luminosity density, Ω_{IR}, for AGN and SFG.

The resulting total luminosity density (Ω_{IR}) is, Ω^{SFG}_{IR}=$5.9^{+1.4}_{-1.3} \times 10^7$ $L_\odot$Mpc^{-3}, and Ω^{AGN}_{IR}=$1.9^{+0.5}_{-0.7} \times 10^7$ $L_\odot$Mpc^{-3}, as summarized in Table 1. Errors are estimated by varying the fit within 1σ of uncertainty in LFs. The results show that among the total IR luminosity density integrated over all the IR luminosity range, 75% ($\frac{\Omega^{SFG}_{IR}}{\Omega^{AGN}_{IR}+\Omega^{SFG}_{IR}}$) of IR luminosity density is emitted by the SFG, and only 24% ($\frac{\Omega^{AGN}_{IR}}{\Omega^{AGN}_{IR}+\Omega^{SFG}_{IR}}$) is by AGN at z=0.031. The AGN contribution is larger than z=0.0081, however, is still small compared with higher redshift results (Pérez-González et al. 2005; Le Floc'h et al. 2005; Magnelli et al. 2009; Goto et al. 2010a).

Once we have Ω^{SFG}_{IR}, we can estimate star formation density emitted in infrared light. The SFR and L_{IR} is related by the following equation for a Salpeter IMF, ϕ (m) $\propto m^{-2.35}$ between $0.1 - 100 M_\odot$ (Kennicutt 1998).

$$SFR[M_\odot yr^{-1}] = 1.72 \times 10^{-10} L_{IR}[L_\odot] \quad (4)$$

By using this equation, we obtain SFR density = 1.3±0.2 $10^{-2} M_\odot yr^{-1}$.

If we limit our integration to ULIRG luminosity range ($L_{IR} > 10^{12} L_\odot$), we obtain, Ω^{SFG}_{IR}(ULIRG)= $1.4^{+0.2}_{-0.2} \times 10^5$ $L_\odot$Mpc^{-3}, and Ω^{AGN}_{IR}(ULIRG)= $2.5^{+1.3}_{-0.9} \times 10^5$ $L_\odot$Mpc^{-3}. In other words, at ULIRG luminosity range, AGN explain 64% ($\frac{\Omega^{AGN}_{IR}(ULIRG)}{\Omega^{AGN}_{IR}(ULIRG)+\Omega^{SFG}_{IR}(ULIRG)}$) of IR luminosity, again showing the AGN dominance at the bright-end.

Note that Ω^{AGN}_{IR}(ULIRG) larger than Ω^{Total}_{IR}(ULIRG) is apparently inconsistent. This is due to the limitation in extrapolating the double-power law to obtain Ω_{IR}. For example, the AGN LF has a flatter bright-end slope of beta=3.1±0.2 than beta of 3.54±0.09 for total LF. Once extrapolated to larger luminosity at $logL_{IR}$ >12.5, the flatter slope could produce larger Ω_{IR} once integrated even if all the observed data points for AGN are below those of total IR. To obtain more accurate estimate of Ω_{IR} we clearly need data points in larger luminosity range than the AKARI observed. In this paper, we tried to obtain best-estimates of each Ω_{IR} for AGN, SFG, and total. As a result, we caution readers that Ω^{Total}_{IR} is not necessarily the algebraical sum of Ω^{AGN}_{IR} and Ω^{SFG}_{IR}.

In the LIRG luminosity ($L_{IR} > 10^{11} L_\odot$), results are Ω^{SFG}_{IR}(LIRG)= $2.1^{+0.7}_{-0.8} \times 10^6$ $L_\odot$Mpc^{-3}, and Ω^{AGN}_{IR}(LIRG)= $1.9^{+0.5}_{-0.5} \times 10^6$ $L_\odot$Mpc^{-3}. This shows AGN contribution is already down to 47% ($\frac{\Omega^{AGN}_{IR}(LIRG)}{\Omega^{AGN}_{IR}(ULIRG)+\Omega^{SFG}_{IR}(LIRG)}$) of IR luminosity in the LIRG range.

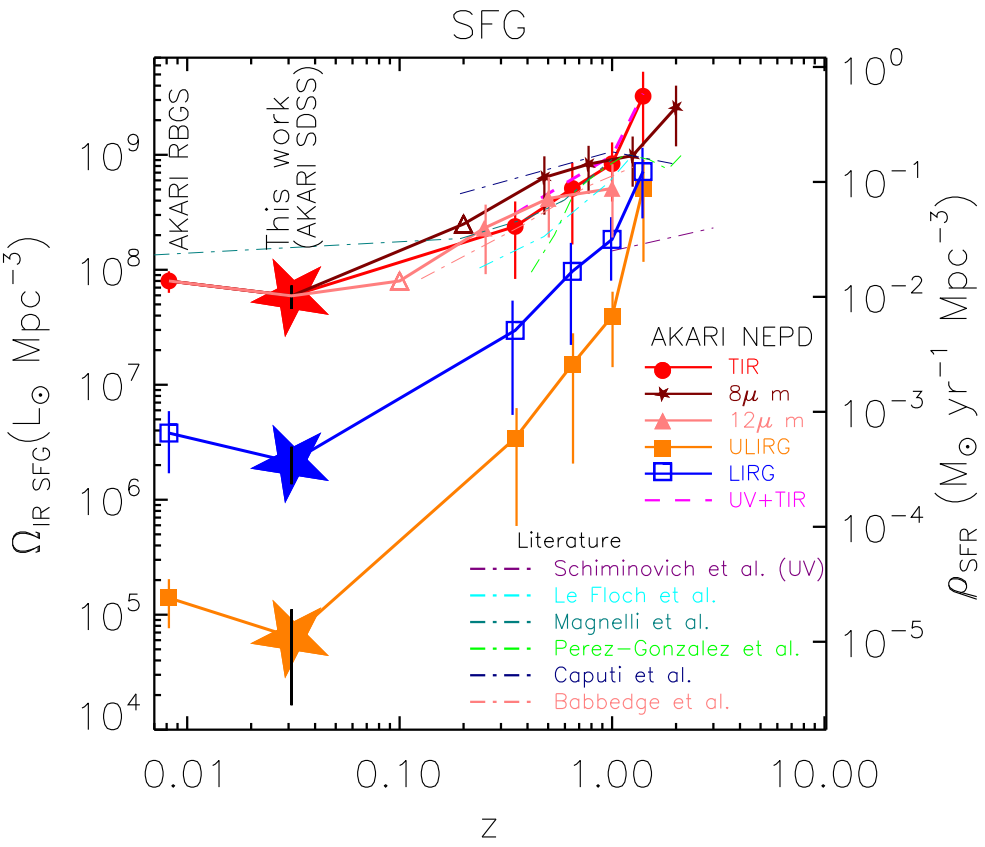

Figure 14. Evolution of IR luminosity density by star-forming galaxies. Results from this work is plotted with stars at z=0.031. The red, blue and orange stars show IR luminosity density from all galaxies, from LIRG only, and from ULIRG only. Higher redshift results in the solid lines are from the AKARI NEP deep field (Goto et al. 2010a). Results at z=0.0082 are from the AKARI RBGS (Goto et al. 2010c). Shown with different colors are IR luminosity density based on IR LFs (red circles), 8μm LFs (stars), and 12μm LFs (filled triangles). The blue open squares and orange filled squares are for only LIRG and ULIRGs, also based on our L_{IR} LFs. Overplotted dot-dashed lines are estimates from the literature: Le Floc'h et al. (2005), Magnelli et al. (2009), Pérez-González et al. (2005), Caputi et al. (2007), and Babbedge et al. (2006) are in cyan, yellow, green, navy, and pink, respectively. The purple dash-dotted line shows UV estimate by Schiminovich et al. (2005). The pink dashed line shows the total estimate of IR (IR LF) and UV (Schiminovich et al. 2005).

4 INFRARED LUMINOSITY DENSITY AND ITS EVOLUTION

4.1 Evolution of Ω_{IR}^{SFG}

We have separated the Ω_{IR}^{SFG} from Ω_{IR}^{AGN}. Now we are ready to examine the evolution of Ω_{SFR} without contribution from AGN. In Fig.14, we plot the evolution of Ω_{IR}^{SFR} as a function of redshift. Higher redshift results are taken from Goto et al. (2010a), who also tried to exclude AGN using SED fitting. Results from the Spitzer survey and GALEX survey are also plotted. The Ω_{IR}^{SFG} shows a strong evolution as a function of redshift. The best-fit linear relation is $\Omega_{IR}^{SFG} \propto (1+z)^{4.1\pm0.4}$. We have removed L_{IR} of optically-classified AGN in this analysis. A caveat in this process, however, is that L_{IR} of optically-selected AGN perhaps includes some IR emission from star-formation in AGN host galaxies. In this sense, Ω_{IR}^{SFG} estimated here is a lower-limit. However, this should not affect Ω_{IR}^{SFG} more than 30% since the Ω_{IR}^{AGN} is smaller than Ω_{IR}^{SFG} by a factor of 3 as we show in the next section.

In comparison, our results are in good agreement with previous works shown in the dash-dotted lines in Fig.14. In the form of $\Omega_{IR} \propto (1+z)^{\gamma}$, Le Floc'h et al. (2005) obtained $\gamma = 3.9 \pm 0.4$, Pérez-González et al. (2005) obtained $\gamma = 4.0 \pm 0.2$, Babbedge et al. (2006) obtained $\gamma = 4.5^{+0.7}_{-0.6}$, Magnelli et al. (2009) obtained $\gamma = 3.6 \pm 0.4$.

Once the IR luminosity density is separated into ULIRG and LIRG contribution, we found $\Omega_{IR}^{SFG}(ULIRG) \propto (1+z)^{10.0\pm0.5}$, and $\Omega_{IR}^{SFG}(LIRG) \propto (1+z)^{6.5\pm0.5}$. $\Omega_{IR}^{SFG}(ULIRG)$ shows more rapid evolution than $\Omega_{IR}^{SFG}(LIRG)$, showing importance of luminous IR sources at high redshift.

4.2 Evolution of Ω_{IR}^{AGN}

In turn, we can also investigate Ω_{IR}^{AGN}. By integrating IR LF_{AGN} in Fig.13, we obtained $\Omega_{IR}^{AGN}=(1.9^{+0.5}_{-0.7}) \times 10^7\ L_{\odot}\mathrm{Mpc}^{-3}$.

In Fig.15, we show the evolution of Ω_{IR}^{AGN}, which shows a strong evolution with increasing redshift. At a first glance, both Ω_{IR}^{AGN} and Ω_{IR}^{SFG} show rapid evolution, suggesting that the correlation between star formation and black hole accretion

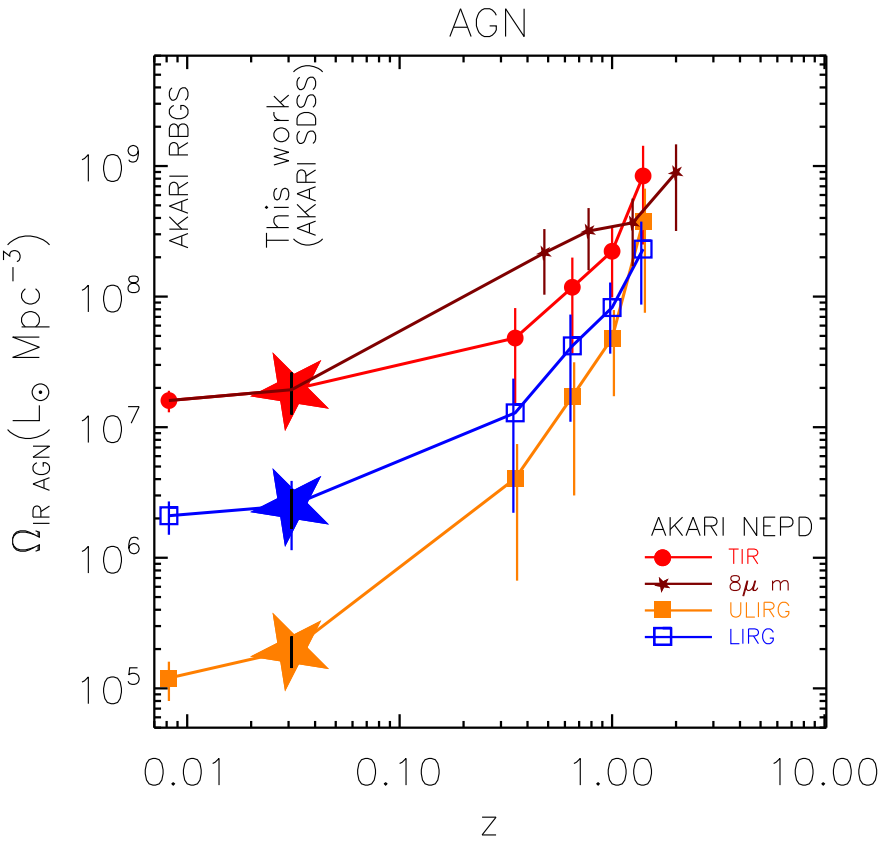

Figure 15. Evolution of IR luminosity density by AGN. Results from this work is plotted with stars at the median redshift of z=0.031. The red, blue and orange points show IR luminosity density from all AGN, from LIRG AGN only, and from ULIRG AGN only. Higher redshift results are from the AKARI NEP deep field (Goto et al. 2010a), with contribution from star forming galaxies removed. Brown triangles are Ω_{IR}^{AGN} computed from the 8μm LFs (Goto et al. 2010a). Results at z=0.0082 are from the AKARI RBGS (Goto et al. 2010c).

rate continues to hold at higher redshifts, i.e., galaxies and black holes seem to be evolving hand in hand. When we fit the evolution with (1+z)$^\gamma$, we found Ω_{IR}^{AGN} $\propto$(1+z)$^{4.1\pm0.5}$. A caveat, however, is that Ω_{IR}^{AGN} estimated in this work likely to include IR emission from host galaxies of AGN, although in optical the AGN component dominates. Therefore, the final conclusion must be drawn from a multi-component fit based on better sampling in FIR by Herschel or SPICA, to separate AGN/SFG contribution to L_{IR}. The contribution by ULIRGs quickly increases toward higher redshift; By z=1.5, it exceeds that from LIRGs. Indeed, we found $\Omega_{IR}^{AGN}(ULIRG)$ $\propto$(1+z)$^{8.7\pm0.6}$ and $\Omega_{IR}^{AGN}(LIRG)$ $\propto$(1+z)$^{5.4\pm0.5}$.

5 SUMMARY

We have cross-correlated the AKARI IR all sky survey with the SDSS to find 2357 IR galaxies with optical spectra. Using AKARI's 6-band IR photometry in 9, 18, 65, 90, 140, and 160μm, we have measured L_{IR} via SED model fitting. The AKARI's 6 bands cover the crucial far-IR wavelengths across the peak of the dust emission, providing us with more accurate L_{IR} measurements than IRAS. By separating SFG/AGN using optical line ratios, we constructed local IR LFs separately for SFG and AGN. We also computed local infrared luminosity density through the derived LFs, and compared Ω_{IR}^{SFG} and Ω_{IR}^{AGN} to those at higher redshifts.

Our findings are as follows.

- The local IR LF with the AKARI data at the median redshift of z=0.031 agrees well with that at z=0.0081, and shows smooth and continuous evolution toward higher redshift results from the AKARI NEP deep field.
- By integrating the IR LF weighted by L_{IR}, we obtain the local cosmic IR luminosity density of Ω_{IR}= $(3.8^{+5.8}_{-1.2})\times10^8$ $L_\odot$Mpc^{-3}.
- The fraction of AGN and composite galaxies show continuous incrase from 25% to 90% at $9 < logL_{IR} <$12.5.
- The SFR based on self-absorption, and extinction corrected $H\alpha$ correlates with L_{IR} for SFGs.
- H$_\alpha$/H$_\beta$ ratio shows a weak increase with L_{IR}, however with a large scatter.
- The $L_{[OIII]}$ correlates well with L_{IR} for AGN.
- The AGN contribution to Ω_{IR} becomes dominant at $L_{IR} > 10^{11}L_\odot$, above the break of the both SFG and AGN IR LFs. At $L_{IR} \leqslant 10^{11}L_\odot$, SFG dominates IR LFs.
- LIRG and ULIRG contribute to Ω_{IR} a little; Only 1.1$\pm$0.1%

of Ω_{IR} is produced by LIRG ($L_{IR} > 10^{11} L_{\odot}$), and only 0.03±0.01% is by ULIRG ($L_{IR} > 10^{12} L_{\odot}$) in the local Universe.

• Compared with high redshift results from the AKARI NEP deep survey, we observed a strong evolution of $\Omega_{IR}^{SFG} \propto (1+z)^{4.1\pm0.4}$, and $\Omega_{IR}^{AGN} \propto (1+z)^{4.1\pm0.5}$.

ACKNOWLEDGMENTS

We thank the anonymous referee for many insightful comments, which significantly improved the paper.

T.G. acknowledges financial support from the Japan Society for the Promotion of Science (JSPS) through JSPS Research Fellowships for Young Scientists.

This research is based on the observations with AKARI, a JAXA project with the participation of ESA.

The authors wish to recognize and acknowledge the very significant cultural role and reverence that the summit of Mauna Kea has always had within the indigenous Hawaiian community. We are most fortunate to have the opportunity to conduct observations from this sacred mountain.

TTT has been supported by Program for Improvement of Research Environment for Young Researchers from Special Coordination Funds for Promoting Science and Technology, and the Grant-in-Aid for the Scientific Research Fund (20740105) commissioned by the Ministry of Education, Culture, Sports, Science and Technology (MEXT) of Japan. TTT has been also partially supported from the Grand-in-Aid for the Global COE Program "Quest for Fundamental Principles in the Universe: from Particles to the Solar System and the Cosmos" from the MEXT.

REFERENCES

Abazajian K. N., et al., 2009, ApJS, 182, 543
Avni Y., Bahcall J. N., 1980, ApJ, 235, 694
Blanton M. R., et al., 2003, AJ, 125, 2348
Babbedge T. S. R., et al., 2006, MNRAS, 370, 1159
Caputi K. I., et al., 2007, ApJ, 660, 97
Chary R., Elbaz D., 2001, ApJ, 556, 562
Dunne L., Eales S. A., 2001, MNRAS, 327, 697
Eisenstein D. J., et al., 2001, AJ, 122, 2267
Goto T., et al., 2010a, A&A, 514, A6
Goto T., et al., 2010b, A&A, 514, A7
Goto T., et al., 2010c, MNRAS in press, arXiv:1008.0859
Goto T., 2005, MNRAS, 360, 322
Gruppioni C., et al., 2010, A&A, 518, L27
Hatziminaoglou E., et al., 2010, A&A, 518, L33
Ishihara D., et al., 2010, A&A, AKARI special issue in press
Jeong W.-S., et al., 2007, PASJ, 59, 429
Kauffmann G., et al., 2003, MNRAS, 346, 1055
Kartaltepe J. S., et al., 2010, ApJ, 709, 572
Kennicutt R. C., Jr., 1998, ARA&A, 36, 189
Kewley L. J., Dopita M. A., Sutherland R. S., Heisler C. A., Trevena J., 2001, ApJ, 556, 121
LaMassa S. M., Heckman T. M., Ptak A., Martins L., Wild V., Sonnentrucker P., 2010, ApJ, 720, 786
Le Floc'h E., et al., 2005, ApJ, 632, 169
Magnelli B., Elbaz D., Chary R. R., Dickinson M., Le Borgne D., Frayer D. T., Willmer C. N. A., 2009, A&A, 496, 57
Murakami H., et al., 2007, PASJ, 59, 369
Pérault M., 1987, PhDT,
Pérez-González P. G., et al., 2005, ApJ, 630, 82
Pier J. R., Munn J. A., Hindsley R. B., Hennessy G. S., Kent S. M., Lupton R. H., Ivezić Ž., 2003, AJ, 125, 1559
Pozzi F., et al., 2004, ApJ, 609, 122
Pozzi F., et al., 2010, A&A, 517, A11
Rodighiero G., et al., 2010, A&A, 515, A8
Rush, B., Malkan, M., Spinoglio, L.,1993, ApJS, 89, 1
Sajina A., et al., 2008, ApJ, 683, 659
Sanders D. B., Mazzarella J. M., Kim D.-C., Surace J. A., Soifer B. T., 2003, AJ, 126, 1607
Saunders W., Rowan-Robinson M., Lawrence A., Efstathiou G., Kaiser N., Ellis R. S., Frenk C. S., 1990, MNRAS, 242, 318
Schawinski K., et al., 2010, ApJ, 711, 284
Schiminovich D., et al., 2005, ApJ, 619, L47
Schmidt M., 1968, ApJ, 151, 393
Serjeant S., et al., 2001, MNRAS, 322, 262
Shao L., et al., 2010, A&A, 518, L26
Smolčić V., 2009, ApJ, 699, L43
Spinoglio L., Malkan M. A., 1989, ApJ, 342, 83
Strauss M. A., et al., 2002, AJ, 124, 1810
Symeonidis M., Page M. J., Seymour N., Dwelly T., Coppin K., McHardy I., Rieke G. H., Huynh M., 2009, MNRAS, 397, 1728
Takeuchi T. T., Yoshikawa K., Ishii T. T., 2000, ApJS, 129, 1
Takeuchi T. T., Ishii T. T., Dole H., Dennefeld M., Lagache G., Puget J.-L., 2006, A&A, 448, 525
Treister E., Urry C. M., Virani S., 2009, ApJ, 696, 110
Yamamura I., et al., 2009, AIPC, 1158, 169
Yuan T.-T., Kewley L. J., Sanders D. B., 2010, ApJ, 709, 884
Zhu Y.-N., Wu H., Cao C., Li H.-N., 2008, ApJ, 686, 155
Sutherland W., Saunders W., 1992, MNRAS, 259, 413